Improving timing sensitivity in the microhertz frequency regime: limits from PSR J1713+0747 on gravitational waves produced by supermassive black hole binaries

B. B. P. Perera,[1]★ B. W. Stappers,[1]★ S. Babak,[2,3]★ M. J. Keith,[1] J. Antoniadis,[4]
C. G. Bassa,[5] R. N. Caballero,[4] D. J. Champion,[4] I. Cognard,[6,7] G. Desvignes,[4]
E. Graikou,[4] L. Guillemot,[6,7] G. H. Janssen,[5,8] R. Karuppusamy,[4] M. Kramer,[1,4]
P. Lazarus,[4] L. Lentati,[9] K. Liu,[4] A. G. Lyne,[1] J. W. McKee,[1,4] S. Osłowski,[4,10,11]
D. Perrodin,[12] S. A. Sanidas,[1,13] A. Sesana,[14] G. Shaifullah,[4,5,11] G. Theureau,[6,7,15]
J. P. W. Verbiest[4,11] and S. R. Taylor[16]

[1]*Jodrell Bank Centre for Astrophysics, School of Physics and Astronomy, The University of Manchester, Manchester M13 9PL, UK*
[2]*APC, Univ. Paris Diderot, CNRC/IN2P3, CEA/Irfu, Obs. de Paris, Sorbonne Paris Cite, France*
[3]*Moscow Institute of Physics and Technology, Dolgoprudny, Moscow region, Russia*
[4]*Max-Planck-Institut für Radioastronomie, Auf dem Hügel 69, D-53121 Bonn, Germany*
[5]*ASTRON, the Netherlands Institute for Radio Astronomy, Postbus 2, NL-7990 AA Dwingeloo, the Netherlands*
[6]*Laboratoire de Physique et Chimie de l'Environnement et de l'Espace LPC2E CNRS-Université d'Orléans, F-45071 Orléans, France*
[7]*Station de radioastronomie de Nançay, Observatoire de CNRS/INSU, F-18330 Nançay, France*
[8]*Department of Astrophysics/IMAPP, Radboud University, P.O. Box 9010, NL-6500 GL Nijmegen, the Netherlands*
[9]*Astrophysics Group, Cavendish Laboratory, JJ Thomson Avenue, Cambridge CB3 0HE, UK*
[10]*Centre for Astrophysics and Supercomputing, Swinburne University of Technology, Post Box 218 Hawthorn, VIC 3122, Australia*
[11]*Fakultät für Physik, Universität Bielefeld, Postfach 100131, D-33501Bielefeld, Germany*
[12]*INAF-Osservatorio Astronomico di Cagliari, via della Scienza 5, I-09047 Selargius (CA), Italy*
[13]*Anton Pannekoek Institute for Astronomy, University of Amsterdam, Science Park 904, NL-1098 XH Amsterdam, the Netherlands*
[14]*School of Physics and Astronomy, University of Birmingham, Edgbaston, Birmingham B15 2TT, UK*
[15]*Laboratoire Univers et Théories LUTh, Observatoire de Paris, CNRS/INSU, Université Paris Diderot, 5 place Jules Janssen, F-92190 Meudon, France*
[16]*Jet Propulsion Laboratory, California Institute of Technology, Pasadena, CA 91109, USA*

ABSTRACT

We search for continuous gravitational waves (CGWs) produced by individual supermassive black hole binaries in circular orbits using high-cadence timing observations of PSR J1713+0747. We observe this millisecond pulsar using the telescopes in the European Pulsar Timing Array with an average cadence of approximately 1.6 d over the period between 2011 April and 2015 July, including an approximately daily average between 2013 February and 2014 April. The high-cadence observations are used to improve the pulsar timing sensitivity across the gravitational wave frequency range of $0.008-5\,\mu$Hz. We use two algorithms in the analysis, including a spectral fitting method and a Bayesian approach. For an independent comparison, we also use a previously published Bayesian algorithm. We find that the Bayesian approaches provide optimal results and the timing observations of the pulsar place a 95 per cent upper limit on the sky-averaged strain amplitude of CGWs to be $\lesssim 3.5 \times 10^{-13}$ at a reference frequency of 1 µHz. We also find a 95 per cent upper limit on the sky-averaged strain amplitude of low-frequency CGWs to be $\lesssim 1.4 \times 10^{-14}$ at a reference frequency of 20 nHz.

Key words: gravitational waves – binaries: general – stars: black holes – stars: neutron – pulsars: individual: PSR J1713+0747 – quasars: supermassive black holes.

★ E-mail: bhakthiperera@gmail.com (BP) Ben.Stappers@manchester.ac.uk
(BS) stas@apc.in2p3.fr (SB)

1 INTRODUCTION

Millisecond pulsars (MSPs) are old neutron stars that are spun up to periods $\lesssim 30$ ms during a mass accretion phase in binary systems through a so-called recycling process (Alpar et al. 1982; Radhakrishnan & Srinivasan 1982). They are among the most stable known rotators in the universe and the long-term stability, on a time-scale of >10 yr, of the rotation of some of them is comparable to that of an atomic clock (e.g. Petit & Tavella 1996; Hobbs et al. 2012). Due to their high rotational stability, the timing measurements of MSPs can be obtained with a significant accuracy (e.g. Kaspi, Taylor & Ryba 1994). Therefore, pulsars have been identified as excellent tools for searching for gravitational waves (GWs) (see Detweiler 1979; Hellings & Downs 1983; Jenet et al. 2005).

Pulsar timing is sensitive to low-frequency GWs, from nHz to μHz (see Detweiler 1979; Hellings & Downs 1983; Jenet et al. 2005), the natural frequency range of inspiralling supermassive black hole binaries (SMBHBs). Forming as a consequence of galaxy mergers, SMBHBs are expected to form frequently across cosmic history (e.g. Volonteri, Haardt & Madau 2003). The superposition of GW signals from this cosmic population results in a stochastic GW background (Rajagopal & Romani 1995; Jaffe & Backer 2003; Sesana, Vecchio & Colacino 2008), although particularly nearby massive systems are likely to result in individually resolvable signals rising above the background level (Sesana, Vecchio & Volonteri 2009). The lower frequency limit of GWs that pulsar timing is sensitive to is $1/T_{obs}$, where T_{obs} is the total observation span, indicating that a longer time-baseline of data helps to probe the low-frequency GWs. The upper frequency limit depends on the data sampling pattern since the observations are not evenly sampled. Most of the previous pulsar-based GW studies have used the traditional averaged Nyquist frequency $N/(2T_{obs})$ as the upper limit, where N is the number of observations (e.g. Yardley et al. 2010; Arzoumanian et al. 2014; Yi et al. 2014; Zhu et al. 2014; Babak et al. 2016). To be consistent with previous studies and compare the results, we restrict our search analysis to the same frequency range. We note that the upper frequency limit for an unevenly sampled data set can be much larger than the averaged Nyquist frequency (see Eyer & Bartholdi 1999; VanderPlas 2017), but determining the sensitivity in this frequency range is complicated. In order to probe these low-frequency GWs, high-precision timing of MSPs with sub-microsecond timing accuracy is essential. Pulsar Timing Arrays (PTAs) – the European PTA (EPTA; Desvignes et al. 2016), the Parkes PTA (PPTA; Reardon et al. 2016), and the North American Nanohertz Observatory for Gravitational Waves (NANOGrav; Arzoumanian et al. 2015) – provide a unique way to obtain such a high timing accuracy by observing a collection of highly stable MSPs with good cadence over a long-term period. The International PTA (IPTA), a collaboration of the three individual PTAs, observes about 50 MSPs in total with a time baseline range of $\sim (4.5-27)$ yr and an approximately weekly to monthly cadence, including short-term daily observation campaigns (see Verbiest et al. 2016).

The limits on the amplitude, or the strain, of GWs produced by individual SMBHBs have been previously investigated through pulsar timing in several studies (e.g. Lommen & Backer 2001; Jenet et al. 2004). Babak et al. (2016) used 41 MSPs in the first EPTA data release (Desvignes et al. 2016) and estimated the sky-averaged strain amplitude of continuous gravitational waves (CGWs) to be in the range of $(0.6-1.5) \times 10^{-14}$ at a frequency of $5-7$ nHz. By using 20 MSPs in the first PPTA data release (Manchester et al. 2013), Zhu et al. (2014) estimated the upper limit on the strain amplitude of CGWs to be 1.7×10^{-14} at a frequency of 10 nHz. Arzoumanian et al. (2014) used the observations of 17 MSPs reported in Demorest et al. (2013) and placed the upper limit on the strain of CGWs to be 3×10^{-14} at a frequency of 10 nHz.

Using a spectral fitting method, Yardley et al. (2010) constrained the upper limit on the strain amplitude of CGWs to be about $\sim 1 \times 10^{-13}$ at a frequency of ~ 9 nHz based on 18 MSPs observed by the PPTA. Following the same method, Yi et al. (2014) estimated the upper limit on the strain amplitude of CGWs based on high-cadence observations of PSR B1937+21. They found that the timing of this pulsar constrains an upper limit on the strain amplitude of $\lesssim 1.5 \times 10^{-11}$ and $\lesssim 5 \times 10^{-14}$ at 10^{-7} Hz for random and optimal source location and polarization of individual GW sources, respectively. In the timing analysis, they noticed an unmodelled periodic noise in the timing residuals (i.e. the difference between the observed and model-predicted time of arrivals of pulses) of PSR B1937+21 with an amplitude of 150 ns at a frequency of 3.4 yr^{-1}. Yi et al. (2014) subtracted this periodic signal by fitting a sinusoid and then used the whitened residuals in the GW search analysis. It has been previously reported in other studies that this pulsar exhibits a high level of red timing noise (see Caballero et al. 2016; Lentati et al. 2016) and a significant dispersion measure (DM) variation (e.g. Kaspi et al. 1994; Manchester et al. 2013; Arzoumanian et al. 2015; Desvignes et al. 2016), where DM accounts for the frequency-dependent time delay of the radio pulses due to electrons in the interstellar medium along the line of sight. Therefore, the noise and the DM variation of the pulsar may have perhaps generated this particular periodic signal that was seen in the data. Babak et al. (2016) excluded PSR B1937+21 in their GW analysis due to its complicated high level of timing noise. We note that PSR J1713+0747 exhibits a much lower level of timing noise and DM variation across our observation time span (see Arzoumanian et al. 2015; Desvignes et al. 2016). We thus emphasize that PSR J1713+0747 is a better choice compared to PSR B1937+21 for these types of single-pulsar timing-based GW search analyses. We also note that single-pulsar GW search analyses cannot conclusively detect GWs, rather produce upper limits on strain amplitudes.

PSR J1713+0747 is one of the most precisely timed pulsars by PTAs (Arzoumanian et al. 2015; Desvignes et al. 2016; Reardon et al. 2016). It is regularly observed by all the telescopes involved in PTAs, providing a timing stability of ~ 100 ns based on the recent NANOGrav data release which contains over 9 yr of observations (Arzoumanian et al. 2015). Zhu et al. (2015) reported a timing stability of ~ 92 ns based on 21 yr of observations of the pulsar. Shannon & Cordes (2012) investigated the stability of the pulsar and reported that single pulses show an rms phase fluctuation (the so-called pulse jitter) of ~ 40 ns, which limits the timing precision. Recently, Liu et al. (2016a) analysed the single pulses of the pulsar in detail with data collected by the Large European Array for Pulsars (LEAP; Bassa et al. 2016) project and confirmed that the pulsar shows two modes of systematic subpulse drifting (Edwards & Stappers 2003). The IPTA undertook a 24 hcontinuous global observation campaign of this pulsar using nine telescopes around the world (Dolch et al. 2014). Dolch et al. (2016) showed that the data set in this campaign is sensitive to CGWs with a frequency between 0.01 and 1 mHz. Following Yardley et al. (2010), Dolch et al. (2016) estimated the upper limit on the strain amplitude of CGWs produced by the sources located in the direction of the pulsar to be $\sim 10^{-11}$ at a frequency of 0.01 mHz.

The high-cadence observations are important to understand the noise, and the GW signal if it is present, in pulsar timing data.

Since the observations are unevenly sampled, decreasing the relative cadence of the data will increase the noise level across the power spectrum of the timing residuals. The paper is organized as follows. In Section 2, we present our observations and data processing. We describe the timing analysis of the pulsar in Section 3 and present our timing measurements and residuals. We then present our analysis carried out to obtain the upper limit on the strain amplitude of CGWs in Sections 4.1 and 4.2 using a spectral fitting and a Bayesian approach, respectively. For an independent comparison, we use the algorithm described in Babak et al. (2016) on our data set and present the results in Section 4.3. We apply our limits on SMBHB candidates in Section 4.4 and investigate any possibilities of detecting them. Finally in Section 5, we summarize our results.

2 OBSERVATIONS AND DATA PROCESSING

PSR J1713+0747 was observed using the Lovell Telescope (LT) at the Jodrell Bank Observatory between 2011 April and 2015 July with an average cadence of about 4.5 d. Between 2013 February and 2014 April, the pulsar was observed more frequently with an average cadence of approximately every 2 d. All the LT observations were carried out at *L*-band (with a centre frequency of 1532 MHz) and the data were recorded using the 'ROACH' pulsar backend (see Bassa et al. 2016). In addition to these high-cadence LT observations, we included the observations of the pulsar obtained from three other telescopes – Effelsberg Telescope (EFF) in Germany, Nançay Radio Telescope (NRT) in France, and Westerbork Synthesis Radio Telescope (WSRT) in the Netherlands – in the analysis to further improve the cadence. The EFF observations were recorded using the 'PSRIX' backend (see Lazarus et al. 2016) and carried out at two centre frequencies, 1347 and 2627 MHz. Both single- and multi-beam *L*-band receivers were used at EFF alternatively throughout our observation time span. The NRT observations were made at centre frequencies of 1484, 1524, and 2539 MHz using the 'NUPPI' backend (see Cognard & Theureau 2006; Cognard et al. 2013). The WSRT observations in this analysis were recorded using the 'PuMa II' backend (see Karuppusamy, Stappers & van Straten 2008) and observed at three centre frequencies 350, 1380, and 2200 MHz. All these backends used DSPSR to perform coherent dedispersion and folding (van Straten & Bailes 2011). We note that these observations were obtained using newer backends and are different from the data sets reported in the EPTA data release (Desvignes et al. 2016). To be consistent with all observations, we selected the beginning and the end time of each data set to be equal to that of the LT observations, but we note that the NRT observations started four months after the beginning of the LT observations. The details of the bandwidths, data span, and the number of observations in each data set is given in Table 1. Combining the data from all four telescopes, 952 observation epochs were included in our analysis with a resulting average cadence of about 1.6 d. We also note that the combination of data from other telescopes improved the average cadence of the pulsar to approximately daily within the period between 2013 February and 2014 April, including 420 time of arrivals (TOAs) in total, in which it was monitored more frequently using the LT.

We processed the data using the pulsar analysis software package PSRCHIVE[1] (Hotan, van Straten & Manchester 2004; van Straten, Demorest & Oslowski 2012). PSR J1713+0747 is well known to show a frequency-dependent pulse profile shape variation (see Dolch et al. 2014; Arzoumanian et al. 2015; Zhu et al. 2015), even within a

frequency range of a wide-band receiver (∼400 MHz). This may add an extra uncertainty in the measured TOA if it is obtained through the standard bandwidth-averaged TOA generating method (Taylor 1992). We also note that the scintillation of the pulsar may lead to significant changes in the bandwidth-averaged pulse profile shape due to attenuation of the intensity of the different parts of the frequency band in different observations. Therefore, we use broad-band TOA measurement techniques (see Liu et al. 2014; Pennucci, Demorest & Ransom 2014) on LT and NRT observations. Each epoch was first folded for the entire observation duration using a previously published timing model of the pulsar (Desvignes et al. 2016), while keeping the full frequency resolution across the bandwidth. This gives better signal to noise (S/N) in frequency-channel-dependent pulse profiles. We then sum neighbouring frequency channels together to form eight equal width sub-bands to further improve the S/N. We then use the software[2] introduced in Pennucci et al. (2014) along with 2D eight sub-band noise-free templates to generate TOAs. The telescope-dependent 2D templates were created by using the results of the frequency-dependent pulse profile evolution analysis (Perera et al. in preparation) which was based on the high-resolution observations reported in Dolch et al. (2014). We note that these TOAs improved the weighted rms of the timing residuals of LT observations alone by a factor of 2 compared to that obtained using the standard bandwidth-averaged TOA method (Taylor 1992).

The EFF and WSRT backends use bandwidths a factor of more than 2 smaller (see Table 1) and, therefore, the frequency-dependent profile variation becomes less significant. Thus, we use the standard technique (Taylor 1992) for the remaining data.

3 TIMING THE PULSAR

We fit a previously published timing model (Desvignes et al. 2016) to our observed TOAs and update the solution by minimizing the chi-square of timing residuals using the pulsar timing software package TEMPO2 (Edwards, Hobbs & Manchester 2006; Hobbs, Edwards & Manchester 2006). Since the pulsar is in a binary orbit, the timing model includes Keplerian and post-Keplerian (PK) parameters (see Lorimer & Kramer 2005). We combine TOAs from different telescopes/backends by fitting for time offsets or 'JUMPs' in the timing model to account for any systemic delays between the data sets (e.g. Verbiest et al. 2016). Note that some of our observations were obtained simultaneously using all/several telescopes as a part of LEAP observations (Bassa et al. 2016). Therefore, these simultaneous observations further help in constraining the 'JUMPs' between the relevant data sets in the timing analysis. We note that the interferometric delay measurements between telescopes were not used for these LEAP observations to correct their relative time offsets. We determine the white noise of the pulsar by using the 'TEMPONEST'[3] (Lentati et al. 2014) plugin that is based on a Bayesian analysis. We include white noise parameters EFAC, E_f, and EQUAD, E_q, for each telescope/backend separately in our timing model, which are related to a TOA with uncertainty σ_t in microseconds as $\sigma = \sqrt{E_q^2 + E_F^2 \sigma_t^2}$ (see Lentati et al. 2014; Verbiest et al. 2016). We use uniform and log-uniform prior distributions for EFACs and EQUADs in the fit, respectively. We note that our parallax measurement is barely consistent with those reported in other studies (see Zhu et al. 2015; Desvignes et al. 2016; Verbiest et al. 2016). This could be due to

---

[1] http://psrchive.sourceforge.net/

[2] https://github.com/pennucci/PulsePortraiture
[3] https://github.com/LindleyLentati/TempoNest

Table 1. Details of observations used in the analysis. Two 1.347 GHz Effelsberg data sets have been included in the analysis: the data obtained using the multibeam receiver (denoted as '^{m}') and the single-beam receiver (denoted as '^{s}'). The observation length varies and typical values for data sets are given. In total, 952 observation epochs were included in the analysis, resulting in an average cadence of about 1.6 d. The last column shows EFAC and $\log_{10}$[EQUAD(s)] determined for each data set in the timing model given in Table 2.

Data set	Backend	Centre freq (MHz)	Bandwidth (MHz)	Channel size (MHz)	Phase bins	Obs. length (min)	Data span	No. of TOAs	E_f, $\log_{10}[E_q(s)]$
LT	ROACH	1532	400	1	2048^a	10/30/60	4/2011–7/2015	336	1.00, −6.81
NRT	NUPPI	1484	512	4	2048	42	8/2011–7/2015	193	1.23, −6.98
		1524	512	16	2048	45	1/2013–5/2015	20	1.11, −7.31
		2539	512	4	2048	52	8/2011–12/2014	37	1.34, −6.57
EFF	PSRIX	1347^m	200	1.56	1024	28	4/2011–5/2015	56	1.25, −6.59
		1347^s	200	1.56	1024	28	5/2011–5/2013	27	1.42, −6.83
		2627	200	1.56	1024	30	4/2011–6/2015	41	1.06, −6.22
WSRT	PuMaII	350	70	0.156	256	25/40/60	4/2011–7/2015	87	1.11, −9.80
		1380	160	0.312	512	25/45	4/2011–7/2015	123	0.97, −6.47
		2200	160	0.312	512	25/40	4/2011–12/2014	32	0.67, −7.09

Note. ^{a}Note that there were only 512 pulse phase bins in the early LT observations (i.e. before 2011 July – MJD 55754). Therefore, we fit for an additional 'JUMP' in the timing analysis to correct for the time delay of these TOAs.

different data lengths used in different analyses (e.g. 4.3 yr of data in our work compared to 17.7 yr of data in Desvignes et al. 2016), or some covariance between parameters. Therefore, we use their parallax of 0.90(3) and keep it fixed.

The observing frequencies of our data sets span ∼350−2627MHz (see Table 1). This broad frequency range allows us to fit for the DM and its first two time derivatives, $\dot{DM}(\equiv dDM/dt)$ and $\ddot{DM}(\equiv d^2DM/dt^2)$, in the timing model, and we measure a $\ddot{DM}$ with a 3.5σ significance. The pulsar showed a significant DM event towards the end of 2008 (see Arzoumanian et al. 2015; Zhu et al. 2015; Desvignes et al. 2016). However, the TOAs in our data sets begin in 2011 and therefore no effect from this event is seen in the analysis and we see no evidence for any subsequent events. The timing residuals shown in Fig. 1 are based on the timing model given in Table 2. We note that these results were obtained without including red and stochastic DM noise modelling of the pulsar in the timing analysis.

The measurements of the two PK parameters, range r and shape s, correspond to the Shapiro delay (i.e. the extra time delay of the signal due to the gravitational potential of the binary companion), which leads to measurements of the mass of the pulsar $m_p = 1.41(6)$ M$_\odot$ and the companion $m_c = 0.301(8)$ M$_\odot$ with a 2σ uncertainty. We find that these measurements are consistent with the values reported in previous studies within their uncertainties (see Zhu et al. 2015; Desvignes et al. 2016; Verbiest et al. 2016).

PSR J1713+0747 exhibits some low-level red noise and stochastic DM noise in longer data sets (e.g. Zhu et al. 2015; Caballero et al. 2016; Lentati et al. 2016). The length of our data set is perhaps not long enough to perform a proper noise analysis of the pulsar to measure the appropriate parameters significantly. However, for comparison, we determine the red and DM stochastic noise parameters of the pulsar based on our data set using 'TEMPONEST' (see Lee et al. 2014; Lentati et al. 2014). We include a power-law DM to model a stochastic DM variation component in addition to $\dot{DM}$ and $\ddot{DM}$ in the timing model. To model an additional achromatic red noise process, we include a power-law red noise model and fit for all white and red noise terms along with the parameters given in the timing model simultaneously. We find that the timing measurements are consistent with those obtained without including these additional noise parameters in the timing model. We find the amplitude and the spectral index of the power-law DM

variation are $\log A_{DM} = -14.4 \pm 2.5$ and $\gamma_{DM} = 2.3 \pm 1.8$, respectively, while those of the power-law red noise of the pulsar are $\log A_{red} = -14.9 \pm 1.7$ and $\gamma_{red} = 2.0 \pm 1.7$, respectively. Note that these noise parameters are poorly constrained due to our short data span, but consistent with those estimated in previous studies for this pulsar within the uncertainties (see Caballero et al. 2016; Desvignes et al. 2016; Verbiest et al. 2016). We estimate the Bayes factor (i.e. $B = evidence[H_1]/evidence[H_0]$, where H_1 is the model including the red and DM stochastic noise and H_0 is the model excluding these noise terms) to be $\log_{10}(B) = 8.8(2)$, indicating that the noise model is preferred (Kass & Raftery 1995).

Note that we use the Solar system ephemeris DE421 model (Folkner, Williams & Boggs 2009) in our timing analysis (see Table 2). For an additional comparison, we use the more recent DE436[4] model in the timing analysis and confirm that the timing and noise parameters are very similar to those obtained with the DE421 model. We also confirm that the GW search results obtained from the two models are similar and consistent with each other.

4 PULSAR SENSITIVITY TO INDIVIDUAL GW SOURCES

The GW signal produced by an SMBHB can be seen in the pulsar timing residuals if the pulsar has a sufficiently precise timing solution and the strain amplitude of the particular GW is large enough to produce a detectable signal in the timing residuals that can be distinguished from the timing noise. The sinusoidal GW signature in timing residuals produced by an SMBHB in a circular orbit has two terms due to its binary evolution, namely the 'Earth term', which has a high-frequency behaviour, and the 'pulsar term', which has a low-frequency behaviour (see Jenet et al. 2004). We use the GW model given in Babak et al. (2016), and briefly describe the relevant expressions here in Appendix A. In this study, we mainly assume non-evolving SMBHBs (i.e. the long-term evolution of the binary is negligible compared to the light traveltime between the pulsar and the Earth), so that both the pulsar and Earth terms have the same frequency. We note that the sources might or might not be evolving at the high frequencies relevant to this study depending on
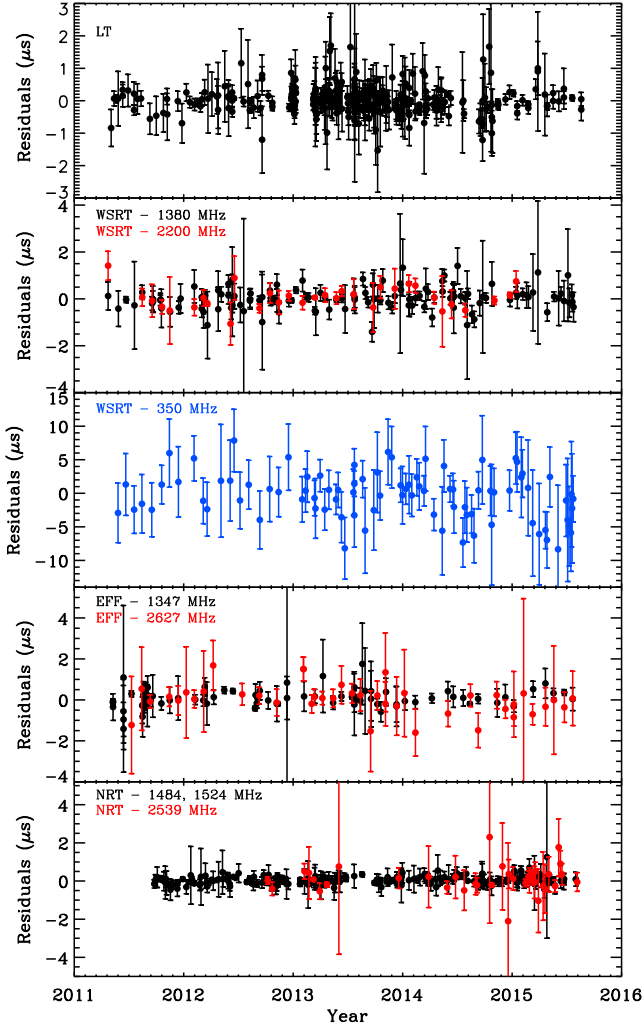
[4]https://naif.jpl.nasa.gov/pub/naif/JUNO/kernels/spk/de436s.bsp.lbl

Figure 1. The timing residuals of PSR J1713+0747. The weighted rms of the residuals is 219 ns. For clarity of the plot, the residuals of the different telescopes are shown in separate panels. The ∼1.4 GHz observations are presented in *black*, and the low- and high-frequency observations are presented in *blue* and *red* colours, respectively. Note that each panel shows different scale in residuals. The average cadence of observations is 1.6 d across the entire data span, while the very-high-cadence observation period between 2013 February and 2014 April achieved an approximately daily observation cadence. Note that the WSRT 350 MHz data set has comparably large uncertainties and thus its weight in the timing analysis is small, although it contributes to the significance of the DM parameters.

the mass of the SMBHB. However, Babak et al. (2016) showed that the GW upper limits are insensitive on the assumed source model (as we will also confirm this in Section 4.3), which indicates this working assumption is valid. By searching for the embedded GW periodic signal in timing residuals, we would be able to estimate the sensitivity limit of the pulsar on the strain amplitude of the CGWs produced by SMBHBs. We followed two different methods. First, we used computationally inexpensive spectral fitting method given in Yardley et al. (2010). We then undertook a computationally expensive more advanced Bayesian approach using the 'TEMPONEST' plugin in TEMPO2. For an independent comparison, we finally use a previously developed algorithm for the first EPTA data release based on Bayesian analysis (Babak et al. 2016), including evolving SMBHBs. We find both Bayesian analyses give consistent upper

Table 2. The timing model parameters of PSR J1713+0747 constrained using our data set given in Table 1. The binary parameters were measured using the T2 binary model given in TEMPO2. We keep the parallax fixed at the value 0.90(3) reported in Desvignes et al. (2016). The position, spin frequency, and DM are given for the reference epoch of MJD 56000.

Timing parameter	
Data span (MJD)	55643–57221
Number of TOAs	952
Weighted rms timing residual (μs)	0.219
Reduced χ^2 value	0.97
Right ascension (RA) (J2000)	17:13:49.5340822(7)
Declination (DEC)(J2000)	+07:47:37.48181(2)
Proper motion in RA (mas yr^{-1})	4.913(4)
Proper motion in DEC (mas yr^{-1})	−3.955(8)
Spin frequency, f (s^{-1})	218.811840 381 872 0(3)
Spin frequency 1st time derivative, $\dot{f}$ (s^{-2})	−4.08356(7) × 10^{-16}
Reference epoch (MJD)	56000
Parallax, π (mas)	0.9
Dispersion measure, DM (cm^{-3} pc)	15.99191(4)
Dispersion measure 1st time derivative, DM(cm^{-3} pc yr^{-1})	−1.0(2) × 10^{-4}
Dispersion measure 2nd time derivative, $\ddot{DM}$ (cm^{-3} pc yr^{-2})	2.8(8) × 10^{-5}
Orbital period, P_b (d)	67.8251309805(6)
Epoch of periastron, T_0 (MJD)	48741.9740(2)
Projected semi-major axis, x (lt-s)	32.34241993(5)
Longitude of periastron, ω (deg)	176.201(1)
Orbital eccentricity, e	7.49404(6) × 10^{-5}
Orbital inclination, i (deg)	70.4(8)
Longitude of ascending node, Ω (deg)	96(3)
Companion mass, m_c (M$_\odot$)	0.301(3)
Clock correction procedure	TT(BIPM2015)
Solar system ephemeris model	DE421
Units	TCB

limits on the strain amplitude, while the spectral method does not provide optimal results, rather it provides slightly larger upper limits. As discussed in Ellis, Jenet & McLaughlin (2012), this spectral fitting method is incoherent and thus provides non-optimal results. For completeness, we first discuss the spectral fitting method and then the Bayesian approaches.

4.1 Spectral fitting method

As mentioned before, here we use the spectral fitting method given in Yardley et al. (2010). The definition of the GW signal given in Yardley et al. (2010) [see equation (4) therein] represents a reduced form and thus misses some parameters (e.g. orbital inclination *i*, initial phase ϕ_0 of the GW signal) compared to the full expression given in Appendix A. We notice that this reduced form provides a few factors poor results in the upper limit estimates. Therefore, we use the full GW expression.

We first obtain the power spectrum of the timing residuals of PSR J1713+0747 shown in Fig. 1. The power spectrum of an unevenly sampled data set can be obtained by using the Lomb–Scargle (LS) periodogram (Lomb 1976; Scargle 1982). However, the original LS periodogram does not account for the uncertainties of the data. When generating the power spectrum from timing residuals, it is important to include the uncertainties to avoid any biases of the power in the spectrum to less-weighted residuals. Therefore, we use the Generalized Lomb–Scargle periodogram (GLSP) formalism introduced in Zechmeister & Kürster (2009), which accounts for the uncertainties of the data points by including weights and also fits
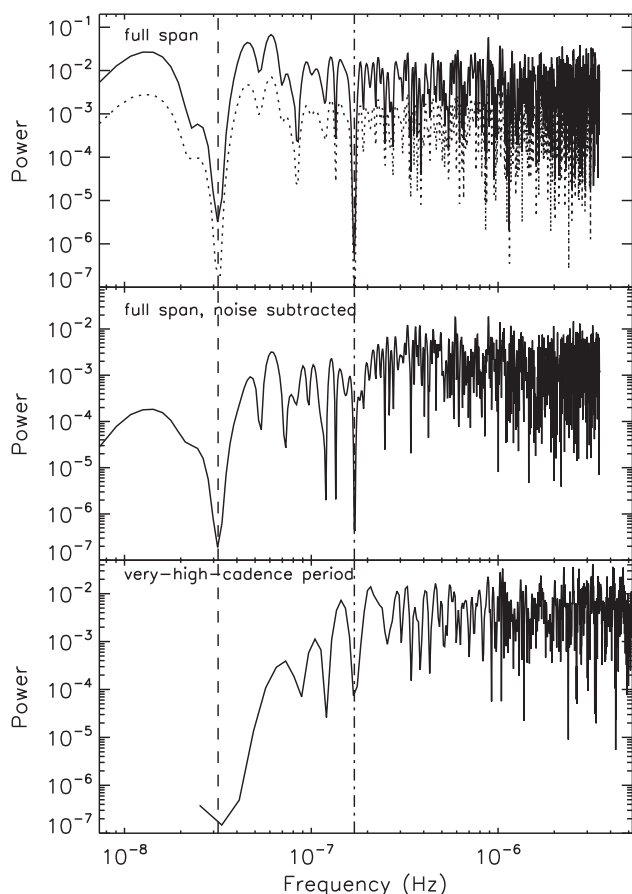
Figure 2. The power spectrum of the timing residuals of the pulsar given in Fig. 1. The *top* panel shows the spectrum generated using the entire data set across the full data span, including (*solid* curve) and excluding (*dotted* curve) the low-frequency WSRT 350 MHz data set. For the clarity of the plot, we shifted the *dotted* curve down by a factor of 0.1. We note that both curves are very similar, indicating that the GLSP method accounts for the less-weighted WSRT 350 MHz data correctly in the periodogram. The *middle* panel represents the power spectrum generated using the timing residuals after subtracting the waveforms of the red and stochastic DM power-law noise terms as described in Section 3. The *bottom* panel shows the spectrum for the very-high-cadence period of the observations after accounting for all noise parameters in the timing model. Note that the upper bound of the frequency range is extended beyond 3.5 μs with this very-high-cadence observations. The *y*-axis represents the normalized power (see Zechmeister & Kürster 2009 for details). The vertical *dashed* and *dash–dotted* lines represent the frequencies of 1 yr^{-1} and the orbital period of 67.8 d of the pulsar, respectively.

for a floating mean. The power spectrum of our timing residuals is given in Fig. 2. We note that since the periodogram is weighted by the uncertainties, the low-frequency WSRT 350 MHz residuals with large uncertainties (see Fig. 1) do not contribute significantly. This can be clearly seen in the *top* panel in Fig. 2, where the spectrum is calculated including (*solid* curve) and excluding (*dotted* curve) the WSRT 350 MHz data, respectively. Note that we shifted the *dotted* curve down by a factor of 0.1 for clarity of the figure.

In contrast to PSR B1937+21 (see Yi et al. 2014), Fig. 2 shows that the timing residuals of PSR J1713+0747 do not present any significant unmodelled periodic signals. However, as mentioned in Section 3, we also estimated DM stochastic and red noise parameters in the timing analysis. For comparison, the middle panel in Fig. 2 shows the power spectrum after subtracting the time-domain

waveforms of these noise terms in the timing model, resulting in a slightly lower spectral power at low frequencies compared to the previous case. The power spectrum of the residuals, after subtracting the waveforms of additional DM and red noise terms, on the data within the very high-cadence observing period is shown in the *bottom* panel of Fig. 2. No noticeable red noise is seen within this short, but high-cadence, time span. The significant power drop at the yearly period (i.e. a frequency of $\sim 3 \times 10^{-8}$ Hz) in Fig. 2 is common for all three cases and it is due to fitting for the pulsar position in the timing model. Similarly, the power absorption at $\sim 1.7 \times 10^{-7}$ Hz is due to fitting for the orbital period, $P_b = 67.8$ d.

We then use the same method outlined in previous studies (see Yardley et al. 2010; Yi et al. 2014) to build the detection threshold using the power spectrum of timing residuals. To remove any spurious effects from any apparent unmodelled signals and noise in the timing residuals, we smooth the spectrum given in Fig. 2 (top panel) and fit a polynomial. We find that a third-order polynomial function is sufficient to fit the data. We then scale this polynomial by a factor α in power in the spectrum. It is determined by simulating 10^4 data sets with TOAs having uncertainties of 100 ns and cadence that matches the observed data. We then obtain the power spectrum of each realization and calculate the mean power. We label the mean power of the ith spectrum as m_i. We increase α starting from 1 and count the number of power spectra that have any power value greater than αm_i. We set a 1 per cent false alarm rate and increase α until the number of spectra satisfies this threshold. We find that the best α for our data set is 10.1, and scale the polynomial in power accordingly, in order to build the detection threshold.

We then divide the frequency range of the observed spectrum into 100 equal bins in logspace. We inject the pulsar and Earth terms at the same frequency, according to the model given in Appendix A, for a given h_s in the observed TOAs (see equation A1). We fit our timing model of the pulsar to the new GW-injected TOAs using TEMPO2 and obtain timing residuals. The power spectrum of the timing residuals is then compared with the detection threshold at the given frequency for a detection (see Yardley et al. 2010; Yi et al. 2014 for more details). For each h_s, we perform 1000 trials using randomly selected ϕ_S, θ_S, ϕ_0, ψ, and i and then count the number of detections (see Appendix A for definitions of these parameters). We increase h_s until the signals of 95 per cent of trials are detected and then record the particular h_s as the upper limit for that given frequency bin. We repeat this process for all frequency bins. This gives the 95 per cent upper limit on the sky-averaged strain amplitude of CGWs produced by SMBHBs. We present our upper limit curve in Fig. 3 [see panels (a) and (b)]. For an optimal sky location, we assume all the SMBHBs are located in the direction of the pulsar ($\pm 10°$ in the direction of the pulsar), and repeat the same procedure as before. As shown in the figure, the optimal upper limit is a factor of a few better than the sky-averaged result.

4.2 Bayesian approach using TEMPONEST

The spectral fitting method described above is an incoherent ad hoc method that does not provide optimal results. It does not include the noise processes of the pulsar (i.e. red and DM stochastic noise) and it is not straightforward to implement them in the model. If the noise modelling is included in the analysis, then we need to fit for noise properties each time the GW signal is injected and thus the fitting method becomes computationally inefficient. Therefore, we use the Bayesian approach described in Lentati et al. (2014) where the noise properties of the pulsar are constrained using the 'TEMPONEST' plugin. Since we assume that the GW is produced by
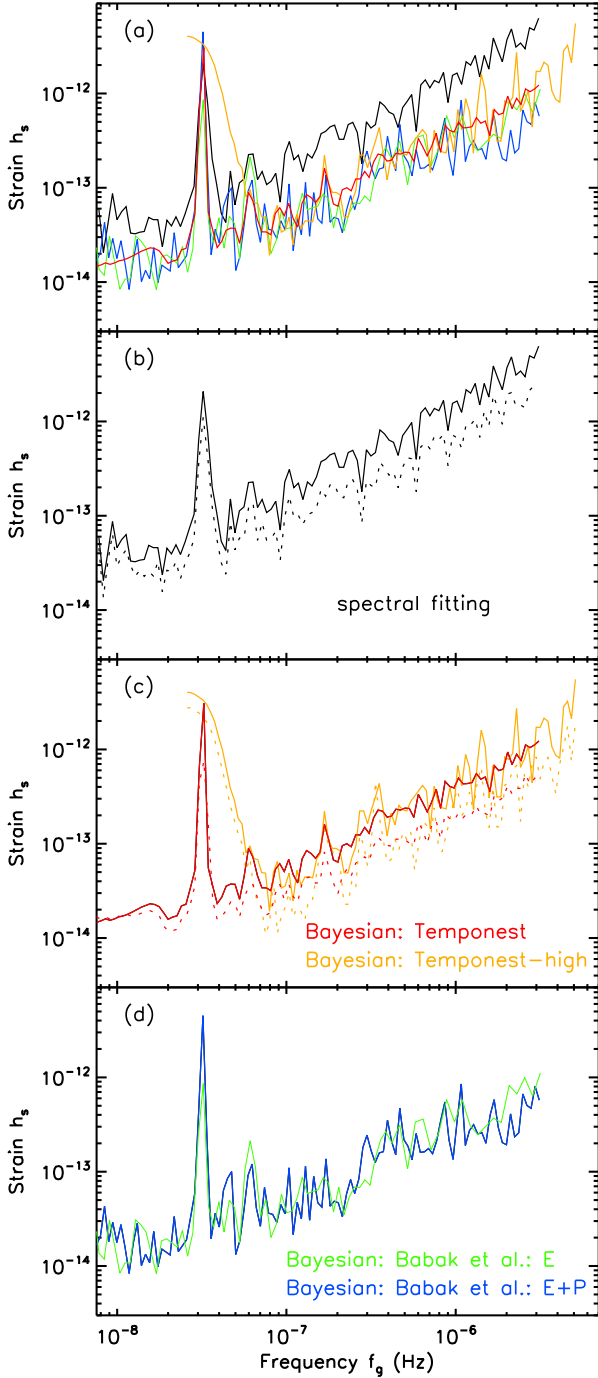
Figure 3. The 95 per cent upper limit on the GW strain amplitude produced by SMBHBs based on the timing observations of PSR J1713+0747. Panel (a) shows the results obtained from all methods described in Section 4. For clarity, we plot the results obtained from each method in the following panels (i.e. from spectral fitting, and Bayesian analysis using TEMPONEST and the algorithm given in Babak et al. 2016, respectively). The *dotted* curves in panels (b) and (c) show the upper limits for the optimal case where all the sources are assumed to be located in the same direction as the pulsar. For comparison, we overplot the upper limits obtained from the data within the high-cadence observation time span between 2013 February and 2014 April [*orange* curves in panel (c)]. Panel (d) shows the upper limits obtained from the algorithm given in Babak et al. (2016) assuming evolving sources, for only the Earth term (*green*) and also for the combined Earth and pulsar terms (*blue*).

an SMBHB in a circular orbit, the signal that can be embedded in the data of a single pulsar is sinusoidal. Therefore, we fit for an additional simple sinusoidal signal while fitting for white noise (i.e. EFACs and EQUADs), and power-law stochastic DM and red noise parameters of the pulsar simultaneously using 'TEMPONEST'. The timing model parameters are marginalized over during the fit (see Lentati et al. 2014 for details about this procedure). The plugin uses Bayesian inference tool MULTINEST to determine this joint parameter space and nested Markov Chain Monte Carlo method for sampling (Feroz & Hobson 2008; Feroz, Hobson & Bridges 2009; Feroz et al. 2013). We use log-uniform prior distributions for amplitudes of the power-law DM stochastic and red noise, and for the frequency of the sinusoidal signal. We use uniform prior distributions for spectral indices of the power-law noise terms, and the amplitude and the phase of the sinusoidal signal. The fit results in approximately 4×10^4 samples in the posterior probability distribution. Each sinusoidal signal sample includes information about its amplitude [$r(t)$], initial phase (ϕ_0), and the frequency (f_g). We then convert the amplitudes of these GW signals to strain amplitudes (h_s) using equation (A1) for randomly selected ϕ_S, θ_S, ϕ_0, ψ, and i (i.e. the polar coordinates of the GW source, initial phase of the signal, GW polarization angle, and orbital inclination, respectively – see Appendix A for details). We divide the frequency range of these GWs (which is equal to the frequency range used in Section 4.1) into 100 equal bins and then obtain the 95 per cent upper limit on the strain amplitude of corresponding signals in each bin. Fig. 3 shows our results [see panels (a) and (c)]. The optimal upper limit is again obtained by considering all sources to be located along the direction of the pulsar [see panel (c) in Fig. 3] as described in Section 4.1.

As mentioned above, Fig. 3 shows that the Bayesian approach provides better limits compared to the spectral fitting method. We also applied this method to the data within the high-cadence observation time span and obtained the upper limit on the strain amplitude [panel (c) of Fig. 3].

4.3 Using previously published Bayesian algorithm

In order to further validate our results, we use the algorithm presented in Babak et al. (2016). In this Bayesian analysis, we use POLYCHORD (Handley, Hobson & Lasenby 2015) to fit for the CGW signal (i.e. h_s, ϕ_S, θ_S, ϕ_0, ψ, i, and f_g) and the noise parameters (i.e. EFACs, EQUADs, power-law stochastic DM, and red noise processes). Similar to the method in Section 4.2, the timing model parameters are marginalized over during the fit. In addition to different tools used in the two Bayesian approaches, Babak et al. (2016) are capable of using both evolving and non-evolving sources in the search analysis, whereas the method in Section 4.2 uses only non-evolving sources. The underlying algorithm utilizes the GW model described in Appendix A, and the details of the fitting procedure is described in Babak et al. (2016) and Taylor (2017). In the search for evolving sources, we use three extra parameters in the model – the chirp mass of the system, distance to the pulsar, and the initial phase of the pulsar term. For the distance to the pulsar, we use the Gaussian prior centred at the best currently known value with the measured uncertainty of 1.05(7) kpc (Chatterjee et al. 2009). As mentioned above, we use POLYCHORD (nested sampling) in this analysis, which is the next incarnation of the MULTINEST. It is supposed to be more robust for the multimodal likelihood surfaces embedded in the large dimensional parameter space and more efficient for some problems. However, we find no benefit of the new implementation, rather both

Table 3. The SMBHB candidates considered in this analysis based on three studies: (1) CRTS (Graham et al. 2015), (2) PTF data base (Charisi et al. 2016), and (3) Pan-STARRS1 Medium Deep Survey (Liu et al. 2015, 2016b). Note that the expected GW frequencies from these sources fall in the regime that our pulsar timing analysis can be probed.

Study	Candidates	z	Period (yr)	Frequency (nHz)
1	111	$0.1-2.7$	$1.8-6.7$	$9.5-35.7$
2	33	$0.3-3.1$	$0.3-2.1$	$29-177$
3	3	$1.2-2.2$	$1.2-1.5$	$41-54$

samplers give very consistent results. The posterior distributions for the noise parameters obtained by the TEMPONEST (described in the Section 4.2) and the method used here are very similar. We also note that the results obtained from evolving and non-evolving sources are consistent with each other. We present the upper limit on the strain amplitude of CGWs in Fig. 3 [see panels (a) and (d)] separately for the Earth term only, as well as for the combined Earth and pulsar terms. Fig. 3 shows that these results are consistent with the results obtained from the Bayesian approach described in Section 4.2.

4.4 Application to proposed SMBHB candidates

It is thought that quasars contain SMBHs and SMBHBs in their nuclei. Although SMBHBs are not resolvable optically by direct imaging, candidates can be identified through periodicity in their optical, radio, and X-ray fluxes. The quadrupole torque produced by a binary induces a periodicity in the accretion flow from a circumbinary disc related to its orbital period (Artymowicz & Lubow 1994; MacFadyen & Milosavljević 2008; Roedig et al. 2011). This might result in periodic luminosity variations (e.g. Sesana et al. 2012). By searching for periodicities in observations of quasars, SMBHB candidates have been identified in many surveys. In this study, we consider those identified by the Catalina Real-time Transient Survey (CRTS) (Graham et al. 2015), Palomar Transient Factory (PTF) data base (Charisi et al. 2016), and Pan-STARRS1 Medium Deep Survey (Liu et al. 2015, 2016b), which identified 111, 33, and 3 candidate SMBHBs, respectively (see Table 3). We note that the periodicities of all these candidate sources are expected to produce GWs in the frequency range between approximately $10^{-8}-10^{-7}$ Hz, which falls into the frequency range that our timing of PSR J1713+0747 can probe. Therefore, we estimated these expected signals [using equation (A10) and assuming equal mass SMBHs (i.e. $q = M_2/M = 1$) in binary systems[1]] and compared them with our timing-derived upper limit on the strain amplitude (see Fig. 4). The lower limit of these expected signals shown in the figure is estimated by assuming a mass ratio of $q = M_2/M_1 = 0.1$. As seen in Fig. 4, the strain amplitudes of the predicted GW signals from these sources are lower (by more than a factor of 4 for the strongest ones) than the sky-averaged sensitivity curve for PSR J1713+0747. We note that none of these candidates are located in the direction of the pulsar. Thus, using the actual sky locations of these sources in the GW search analysis will not improve the sensitivity significantly compared to the sky-averaged sensitivity presented in Fig. 4 (see the dotted curves in Fig. 3 for upper limits based on optimal sky location). This indicates that we cannot expect to detect GW signals produced by these candidates in our timing results yet.
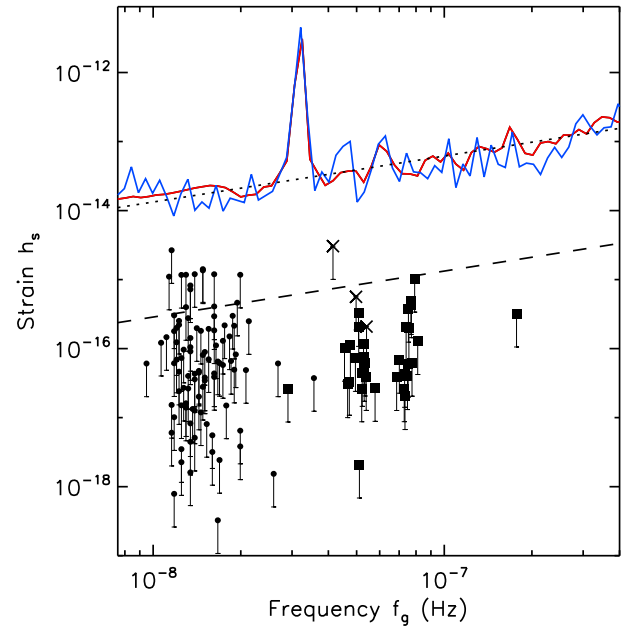

Figure 4. The 95 per cent upper limit on the sky-averaged strain amplitude of CGWs. The colour code of the curves is the same as that given in Fig. 3. For clarity, only the limits obtained from Bayesian approaches are plotted. The *dashed* and *dotted* lines show the theoretically expected strain amplitude from SMBHBs with equal masses of 10^9 and 10^8 $M_\odot$ at a distance of the Virgo cluster, 16.5 Mpc, respectively. The *circles*, *squares*, and *crosses* show the expected GW strain amplitude produced by the SMBHB candidates reported in Graham et al. (2015), Charisi et al. (2016), and Liu et al. (2016b), respectively (see Table 3 for more information). Note that the expected strain amplitudes are estimated using equation (A10) given in Appendix A.

5 CONCLUSIONS

We used high-cadence observations of PSR J1713+0747 to place upper limits on the strain amplitude of CGWs produced by individual SMBHBs in circular orbits. Based on the typical frequency range used in previous studies, $1/T_{obs}$ and $N/(2T_{obs})$ (e.g. Yardley et al. 2010; Yi et al. 2014), we used our observations to probe GWs produced within a frequency range between 7.8×10^{-9} and 5×10^{-6} Hz, covering the high-frequency µHz regime. We used three independent methods in the analysis, including a spectral fitting method and more advanced Bayesian approaches. As mentioned in previous studies (see Yardley et al. 2010; Ellis et al. 2012) and also shown in Fig. 3, the spectral fitting method does not provide optimal results due to its simple incoherent fitting procedure and absence of proper noise modelling of the pulsar. We find that the independent Bayesian analyses are consistent, and also about a factor of 5 better compared to the spectral fitting method. Based on our results, we found a 95 per cent upper limit on the sky-averaged strain amplitude of CGWs to be $\lesssim 3.5 \times 10^{-13}$ at a reference frequency of 1 µHz. For an optimal sky location, the 95 per cent upper limit on the strain amplitude is improved to be $\lesssim 2.1 \times 10^{-13}$ at the same reference frequency. We also found that our timing results place upper limits on the sky-averaged and optimal strain amplitude of low-frequency CGWs to be $\lesssim 1.4 \times 10^{-14}$ and $\lesssim 1.1 \times 10^{-14}$ at a reference frequency of 20 nHz, respectively. This low-frequency limit is approximately three orders of magnitude better compared to the result presented in Yardley et al. (2010) for this pulsar. We also compared our limits with the expected GWs produced by SMBHB candidates, and found that the limits are not yet constraining these

sources. However, we will be able to confirm or reject the binary hypothesis for those candidates in the future with better limits including more observations.

Compared to the upper limits of PSR B1937+21 on GWs presented in Yi et al. (2014), our study shows that PSR J1713+0747 provides better sky-averaged upper limits across the entire frequency range. The poor limits of PSR B1937+21 may have been due to excess noise caused by the known significant DM variation and the high level of red noise in the timing data (see Yi et al. 2014; Caballero et al. 2016; Lentati et al. 2016). As mentioned in Section 4.1, we also note that Yi et al. (2014) used a simplified GW model and it worsens the upper limits by factor of a few compared to that obtained from the full definition of the GW model that we used in our study. The impact of the presence of low-frequency noise in the timing data on their sensitivity to the strain amplitude of GWs was investigated by Caballero et al. (2016) using a subset of the EPTA data over a longer time span of about 17 yr. They showed that the sensitivity reduces by a factor of up to ∼5 at nHz frequencies while at the higher frequencies that our data set is most sensitive, the impact of noise is minimal.

In comparison, the sensitivity limits on CGWs estimated in our analysis at low frequencies are consistent in general with those estimated by PTA studies (see Arzoumanian et al. 2014; Zhu et al. 2014; Babak et al. 2016). These PTA studies combined data from several pulsars in their analysis over long-term observations to obtain their sensitivities compared to single-source data over a short-term observation in our analysis. Our study indicates the importance of collecting more high-cadence observations from good pulsars in PTAs to improve the timing precision and then obtain better GW limits even at low frequencies.

The precision of the timing model (improving the TOA uncertainty) can be improved with time by extending the timing baseline, using larger telescopes and modern backends to observe the pulsar (see Lorimer & Kramer 2005). Therefore, in the future, we can improve the timing precision by including more data in our analysis and thus improve the sensitivity limits of pulsar timing to GWs produced by SMBHBs.

REFERENCES

Alpar M. A., Cheng A. F., Ruderman M. A., Shaham J., 1982, Nature, 300, 728
Artymowicz P., Lubow S. H., 1994, ApJ, 421, 651
Arzoumanian Z. et al., 2014, ApJ, 794, 141
Arzoumanian Z. et al., 2015, ApJ, 813, 65
Babak S. et al., 2016, MNRAS, 455, 1665
Bassa C. G. et al., 2016, MNRAS, 456, 2196
Caballero R. N. et al., 2016, MNRAS, 457, 4421
Charisi M., Bartos I., Haiman Z., Price-Whelan A. M., Graham M. J., Bellm E. C., Laher R. R., Márka S., 2016, MNRAS, 463, 2145
Chatterjee S. et al., 2009, ApJ, 698, 250
Choudhury T. R., Padmanabhan T., 2005, A&A, 429, 807
Cognard I., Theureau G., 2006, in On the present and future of pulsar astronomy, 26th meeting of the IAU, Joint discussion 2, 16-17 August, 2006, Prague, Czech Republic
Cognard I., Theureau G., Guillemot L., Liu K., Lassus A., Desvignes G., 2013, in Cambresy L., Martins F., Nuss E., Palacios A., eds, SF2A-2013: Proceedings of the Annual meeting of the French Society of Astronomy and Astrophysics. p. 327
Demorest P. B. et al., 2013, ApJ, 762, 94
Desvignes G. et al., 2016, MNRAS, 458, 3341
Detweiler S., 1979, ApJ, 234, 1100
Dolch T. et al., 2014, ApJ, 794, 21
Dolch T. et al., 2016, J. Phys: Conf. Ser., 716, 012014
Edwards R. T., Stappers B. W., 2003, A&A, 407, 273
Edwards R. T., Hobbs G. B., Manchester R. N., 2006, MNRAS, 372, 1549
Ellis J. A., Jenet F. A., McLaughlin M. A., 2012, ApJ, 753, 96
Eyer L., Bartholdi P., 1999, A&AS, 135, 1
Feroz F., Hobson M. P., 2008, MNRAS, 384, 449
Feroz F., Hobson M. P., Bridges M., 2009, MNRAS, 398, 1601
Feroz F., Hobson M. P., Cameron E., Pettitt A. N., 2013, preprint (arXiv: 1306.2144)
Folkner W. M., Williams J. G., Boggs D. H., 2009, Interplanet. Netw. Prog. Rep., 178, 1
Graham M. J. et al., 2015, MNRAS, 453, 1562
Handley W. J., Hobson M. P., Lasenby A. N., 2015, MNRAS, 453, 4384
Hellings R. W., Downs G. S., 1983, ApJ, 265, L39
Hobbs G. B., Edwards R. T., Manchester R. N., 2006, MNRAS, 369, 655
Hobbs G. et al., 2012, MNRAS, 427, 2780
Hotan A. W., van Straten W., Manchester R. N., 2004, Publ. Astron. Soc. Aust., 21, 302
Jaffe A. H., Backer D. C., 2003, ApJ, 583, 616
Jenet F. A., Lommen A., Larson S. L., Wen L., 2004, ApJ, 606, 799
Jenet F. A., Hobbs G. B., Lee K. J., Manchester R. N., 2005, ApJ, 625, L123
Karuppusamy R., Stappers B., van Straten W., 2008, PASP, 120, 191
Kaspi V. M., Taylor J. H., Ryba M., 1994, ApJ, 428, 713
Kass R. E., Raftery A. E., 1995, J. Am. Stat. Assoc., 90, 773
Komatsu E. et al., 2009, ApJS, 180, 330
Lazarus P., Karuppusamy R., Graikou E., Caballero R. N., Champion D. J., Lee K. J., Verbiest J. P. W., Kramer M., 2016, MNRAS, 458, 868
Lee K. J., Jenet F. A., Price R. H., 2008, ApJ, 685, 1304
Lee K. J., Wex N., Kramer M., Stappers B. W., Bassa C. G., Janssen G. H., Karuppusamy R., Smits R., 2011, MNRAS, 414, 3251
Lee K. J. et al., 2014, MNRAS, 441, 2831
Lentati L., Alexander P., Hobson M. P., Feroz F., van Haasteren R., Lee K. J., Shannon R. M., 2014, MNRAS, 437, 3004
Lentati L. et al., 2016, MNRAS, 458, 2161

Liu K. et al., 2014, MNRAS, 443, 3752
Liu T. et al., 2015, ApJ, 803, L16
Liu K. et al., 2016a, MNRAS, 463, 3239
Liu T. et al., 2016b, ApJ, 833, 6
Lomb N. R., 1976, Ap&SS, 39, 447
Lommen A. N., Backer D. C., 2001, ApJ, 562, 297
Lorimer D. R., Kramer M., 2005, Handbook of Pulsar Astronomy. Cambridge Univ. Press, Cambridge
MacFadyen A. I., Milosavljević M., 2008, ApJ, 672, 83
Manchester R. N. et al., 2013, Publ. Astron. Soc. Aust., 30, e017
Pennucci T. T., Demorest P. B., Ransom S. M., 2014, ApJ, 790, 93
Petit G., Tavella P., 1996, A&A, 308, 290
Radhakrishnan V., Srinivasan G., 1982, Curr. Sci., 51, 1096
Rajagopal M., Romani R. W., 1995, ApJ, 446, 543
Reardon D. J. et al., 2016, MNRAS, 455, 1751
Roedig C., Dotti M., Sesana A., Cuadra J., Colpi M., 2011, MNRAS, 415, 3033
Scargle J. D., 1982, ApJ, 263, 835
Sesana A., Vecchio A., 2010, Phys. Rev. D, 81, 104008
Sesana A., Vecchio A., Colacino C. N., 2008, MNRAS, 390, 192
Sesana A., Vecchio A., Volonteri M., 2009, MNRAS, 394, 2255
Sesana A., Roedig C., Reynolds M. T., Dotti M., 2012, MNRAS, 420, 860
Shannon R. M., Cordes J. M., 2012, ApJ, 761, 64
Stavridis A., Arun K. G., Will C. M., 2009, Phys. Rev. D, 80, 067501
Taylor J. H., 1992, Phil. Trans. R. Soc. A, 341, 117
Taylor S. R., 2017, https://github.com/stevertaylor/NX01, https://doi.org/10.5281/zenodo.250258
van Straten W., Bailes M., 2011, Publ. Astron. Soc. Aust., 28, 1
van Straten W., Demorest P., Oslowski S., 2012, Astron. Res. Technol., 9, 237
VanderPlas J. T., 2018, ApJS, 236, 16
Verbiest J. P. W. et al., 2016, MNRAS, 458, 1267
Volonteri M., Haardt F., Madau P., 2003, ApJ, 582, 559
Yardley D. R. B. et al., 2010, MNRAS, 407, 669
Yi S., Stappers B. W., Sanidas S. A., Bassa C. G., Janssen G. H., Lyne A. G., Kramer M., Zhang S.-N., 2014, MNRAS, 445, 1245
Zechmeister M., Kürster M., 2009, A&A, 496, 577
Zhu W. W. et al., 2015, ApJ, 809, 41
Zhu X.-J. et al., 2014, MNRAS, 444, 3709

APPENDIX A: GW MODEL

The sinusoidal signal produced by a non-evolving GW source in the timing residuals of a pulsar is given by

$$r(t) = r^e(t) - r^p(t_p).\tag{A1}$$

Here, $t_p = t - D(1 + \hat{\Omega} \cdot \hat{p})/c$, where D is the distance to the pulsar, c is the speed of light, $\hat{\Omega}$ is the unit vector along the direction of GW propagation, and $\hat{p}$ is the unit vector along the direction of the radio waves propagating from the pulsar. We use the astrometry-derived pulsar distance of 1.05(7) kpc (Chatterjee et al. 2009), which is consistent with the distance derived from the measured DM and the parallax (see Desvignes et al. 2016). The Earth and pulsar terms are given by

$$r^e(t) = \frac{h_s}{\omega} \{(1 + \cos^2 i) F^+[\sin(\omega t + \phi_0)] + 2 \cos i \, F^\times [\cos(\omega t + \phi_0)]\}\tag{A2}$$

and

$$r^p(t_p) = \frac{h_s}{\omega} \{(1 + \cos^2 i) F^+[\sin(\omega t_p + \phi_0)] + 2 \cos i \, F^\times [\cos(\omega t_p + \phi_0)]\},\tag{A3}$$

where h_s is the strain amplitude of the GW signal, $f_g = \omega/2\pi$ is the frequency of the GW signal, i is the inclination angle of the SMBHB orbit with respect to the line of sight, and ϕ_0 is the initial phase of the signal. The 'antenna beam patterns' are given by

$$F^+ = \frac{1}{2} \frac{(\hat{m} \cdot \hat{p})^2 - (\hat{n} \cdot \hat{p})^2}{1 + \hat{\Omega} \cdot \hat{p}}\tag{A4}$$

and

$$F^\times = \frac{(\hat{m} \cdot \hat{p})(\hat{n} \cdot \hat{p})}{1 + \hat{\Omega} \cdot \hat{p}}.\tag{A5}$$

For a Cartesian coordinate system (x, y, z), we can define all above unit vectors as

$$\hat{m} = (\sin \phi_S \cos \psi - \sin \psi \cos \phi_S \cos \theta_S)\hat{x} - (\cos \phi_S \cos \psi + \sin \psi \sin \phi_S \cos \theta_S)\hat{y} + (\sin \psi \sin \theta_S)\hat{z},\tag{A6}$$

$$\hat{n} = (-\sin \phi_S \sin \psi - \cos \psi \cos \phi_S \cos \theta_S)\hat{x} + (\cos \phi_S \sin \psi - \cos \psi \sin \phi_S \cos \theta_S)\hat{y} + (\cos \psi \sin \theta_S)\hat{z},\tag{A7}$$

$$\hat{\Omega} = -(\sin \theta_S \cos \phi_S)\hat{x} - (\sin \theta_S \sin \phi_S)\hat{y} - \cos \theta_S \hat{z}, \text{ and}\tag{A8}$$

$$\hat{p} = (\sin \theta \cos \phi)\hat{x} + (\sin \theta \sin \phi)\hat{y} + \cos \theta \hat{z},\tag{A9}$$

where θ_S and ϕ_S are the usual polar coordinates of the GW source location in the sky, θ and ϕ are the usual polar coordinates of the pulsar, and ψ is the GW polarization angle. The derivation of the above expressions are given in previous studies in detail (see Lee, Jenet & Price 2008; Sesana & Vecchio 2010; Lee et al. 2011; Zhu et al. 2014; Babak et al. 2016). The GW strain amplitude is defined as

$$h_s = 2 \frac{(GM_c)^{5/3}}{c^4 D_L(z)} (\pi f_g)^{2/3},\tag{A10}$$

where $M_c = (M_1 M_2)^{3/5}(M_1 + M_2)^{-1/5}$ is the chirp mass of the system with individual masses of M_1 and M_2, and G is the gravitational constant. The luminosity distance D_L to the source is given by

$$D_L(z) = (1 + z) \frac{c}{H_0} \int_0^z \frac{dz'}{E(z')},\tag{A11}$$

where z is the redshift to the source, H_0 is Hubble's constant ($=72$ km s^{-1} Mpc^{-1}), and $E(z) = H(z)/H_0 = \sqrt{\Omega_\Lambda + \Omega_m(1 + z)^3}$ (see Stavridis, Arun & Will 2009). We use $\Omega_\Lambda = 0.7$ and $\Omega_m = 0.3$ in this work (see Choudhury & Padmanabhan 2005; Komatsu et al. 2009).

This paper has been typeset from a TEX/LATEX file prepared by the author.